ISSN: 2634 - 8853

Journal of Engineering and Applied Sciences Technology

SCIENTIFIC Research and Community

Review Article

Open Access

Experimental and Numerical Study on Suppression of a Turbulent Fire Via Water Mist

Marianne Houndekon, Hui-Ying Wang*, Bruno Coudour and Jean Pierre Garo

Prime Institute (CNRS-UPR 3346, ENSMA, University of Poitiers) Fluid-Thermal-Combustion Department ENSMA - BP 40109 Téléport 2, 1 Avenue Clément Ader 86961 Futuroscope Chasseneuil Cedex, France

ABSTRACT

The present work provides a detailed experimental and numerical study on fire suppression phenomena via water mist in a buoyant, turbulent diffusion flame representing the key characteristics of a realistic fire. Detailed temperature and species fields in addition to heat transfer are presented at the base region of a heptane medium-scale pool fire during the addition of a water mist. The finely divided water mist (50μm) can't be transported to the fire source due to upward buoyancy-induced flow, and its injection has a combustion-supporting effect. The customarily described well defined structure of the flame does not exist any longer by application of water mist. It is observed that the size and shape of the flame vary randomly and continuously due to sudden and short mist vaporization periods. Reduction in flame-to-liquid surface radiation heat feedback via cooling of thermal plume by water mist does not conduct to extinguishing of a fully developed turbulent fire. This behavior suggests that extinguishment is achieved by total clearance of the liquid surface rather than from the reduction in burning rate of liquid fuel. It is important to realize that the measurements are not instantaneous which are affected by the flame disruption, and only averaged values are provided for comparison with the predicted results.

***Corresponding author**

Hui-Ying Wang, Prime Institute (CNRS-UPR 3346, ENSMA, University of Poitiers) Fluid-Thermal-Combustion Department ENSMA - BP 40109 Téléport 2, 1 Avenue Clément Ader 86961 Futuroscope Chasseneuil Cedex, France.

Received: July 03, 2026; **Accepted:** July 13, 2026; **Published:** July 20, 2026

Keywords: Fire Suppression, Water Mist, Liquid Fuel, Burning Rate, Radiation

Introduction

As an alternative to halogenated alkyl fire extinguishing agents, sprinklers are widely used in industry facilities since it is shown applicable to suppression of gas, liquid and solid combustible fires [1]. During the fire-water interaction period, the fire structure is controlled by many parameters such as water application time, flux density, spray dynamics and droplet size [2]. Understanding the fire spread and suppression mechanisms increases the performance of protection systems to reduce fire damage. For early application in an environment which is not hot enough to result in a strong droplet evaporation, fuel cooling was identified as the main mechanism leading to fire suppression [3]. Reduction in the flame temperature below a critical value necessary to sustain combustion can be achieved thanks to activation of fire suppression system at the early stage of fire growth [4]. A long time is required for the fire suppression via cooling of the fuel surface once the fire is fully developed. In presence of the plume and the flame, only the large droplets in diameter with sufficient momentum can reach the liquid burning surface where droplets either splash or accumulate into a thin liquid film. The fire suppression is significantly affected by airflows produced by natural or forced ventilation in water mist, smoke extraction systems and movement of fire load [5]. The fire suppression performance is achieved when droplets evaporate close to the flame sheet via latent cooling effects [6]. The regimes of flame-spray interaction are strongly affected by transient fire growth and reduction of the burning rate due to surface wetting [7]. About 6-11% of the heat produced by a fire can be removed thanks to droplets evaporation as a function of fire scale [8]. Operating parameters, such as distance between the pool fire and the nozzle, gap of platform, nozzle ejection rate, and water mist particle size primarily affect fire suppression performance [9]. Heat radiation from the fire source can be reduced more effectively when the entire fire extinguishing space is filled by the mist via the atomization effect of high-pressure water mist [10]. Suppression performance of large-scale, turbulent fires via water mist has been investigated without the detailed characterization and controlled conditions necessary for model validation [11, 12].

The objective of the present work is to provide a detailed experimental and numerical study on fire suppression phenomena via water mist in a buoyant, turbulent diffusion flame representing the key characteristics of a realistic fire. From the present work, it is found that water mist application allows to achieve maximum droplet evaporation in the thermal plume over a liquid pool fire. As a result, the water mist can't be transported to the fire source during the fire-water interaction period due to upward buoyancy-induced flow. Reduction in flame-to-liquid surface radiation heat feedback via cooling of thermal plume by water mist does not conduct to extinguishing of a fully developed turbulent fire. Through the analysis on heat release rate, gas temperature, convection/ radiation heat flux and chemical species, it is concluded that in a

hot environment, a consecutive efficient cooling of the thermal plume leads to the fire suppression via dilution thanks to a strong droplet evaporation. Both the complexity required for relation to realistic fire scenarios and the detailed diagnostics required for validation of CFD tool such as FDS have been contained [13].

Experimental Set-Up

Experiments were performed with heptane pool fires, as shown in Fig.1a. Heptane was contained in a circular steel pan, 10 cm deep, with a diameter of 23 cm. During the test, the level was kept constant by means of a gravity liquid feeding system, as schematized in Fig.1b, based on an electronically controlled on/off valve [14]. The fuel supply rate is 0.66 ± 0.05 g/s.

The water mist system used consists of three nozzles which are located symmetrically with respect to the flame axis (120°) and directed toward the fuel surface centre with an angle of 35°. The distance between the nozzles and the liquid surface is 1.29 m with a radial position 0.7 m. The nozzles are twin fluid (water/air) pressure assisted atomizers permitting the control of the droplet size, flow density, and momentum of the mist. The applied air pressure and water flow are chosen in such a way that complete extinguishment does not occur immediately or even does not occur at all. Each nozzle works at a normal operating air-pressure of 1 bar and provides a water mass flow rate of 3.5 g/s. The local speed, particle size and concentration of the droplet were properly scaled by using a laser anemometry system called PDPA (Phase Doppler Particle Analyser). Water mist is delivered as an opposed buoyancy-induced flow, properly oriented with high momentum, in order to push the water vapour formed against the fuel surface. Heptane has a low flash point temperature (-4°C) and high vapour pressure, thus it is difficult to reduce the vapour/air mixture to below its lean flammability limit. This allows to analyse in a long duration, on one hand, the perturbation influence of a water mist addition on the interaction between flame destabilization and extinction, and on the other hand, on the radiant heat feedback over the pyrolysis surface. To measure the radiant heat flux over the fuel surface (below 20 kW/m2), three Gardon-gauge-type radiometers Medtherm are used. Each radiometer was water cooled and equipped with a window to eliminate the conductive and convective components from the flame. The window used is in calcium fluoride with a spectral transmittance between 0.3 and 11.5 μm which covers the spectral range of a luminous flame between 0.5 and 5 μm. The view factor of these radiometers was 150° and uncertainty in heat flux measurements is within 3%. The gas temperature was measured with five thermocouple trees type K of chromel-alumel and 0.5 mm wire which are arranged at intervals of 2.5 cm.

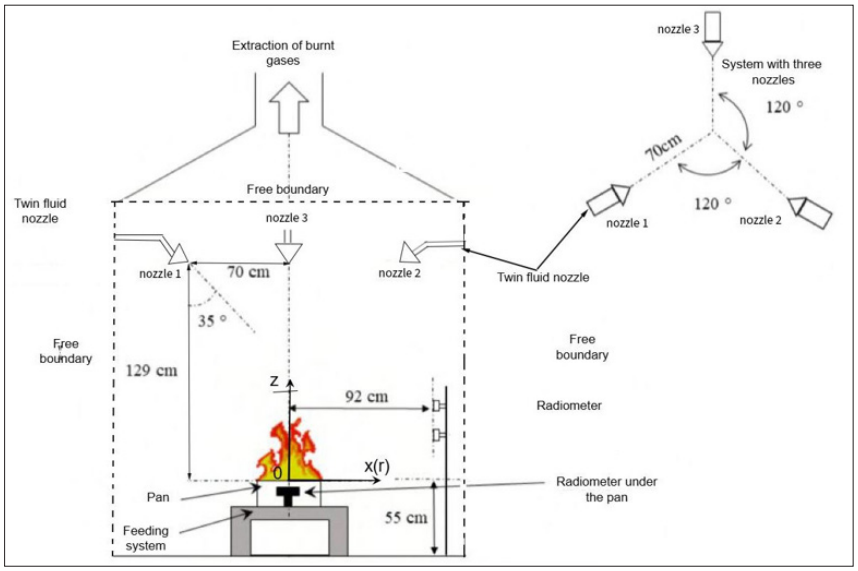

1a) 2D Side View of The Experimental Set Up with a Water Mist System

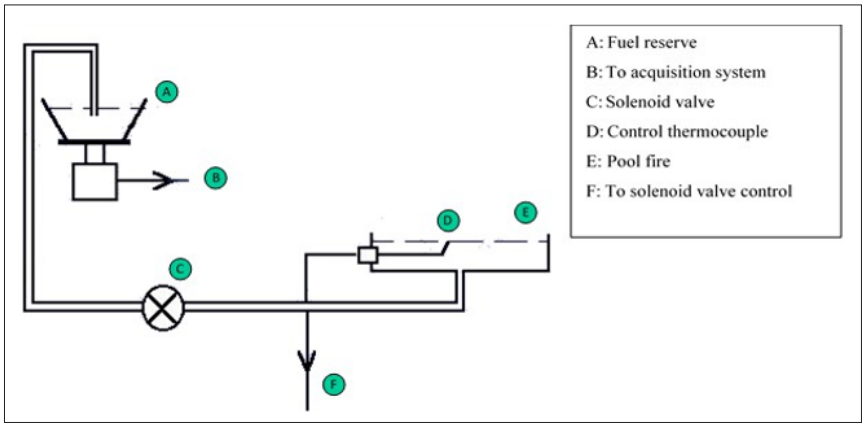

1b) Scheme of a Gravity Liquid Feeding System

Figure 1: Scheme of The Experimental Set Up Consisting of a Water Mist System

Numerical Modelling

Fire Dynamics Simulator (FDS6.7) is used for the simulations conducted throughout this study [13]. In order to reduce calculation time, FDS uses an approximated expression of the Navier-Stokes equations where acoustic waves are filtered whereas it still permits big density and temperature changes. Large Eddy Simulation (LES) and the Lagrangian approach are adopted to describe respectively turbulence and water droplet transport. The hydrodynamic model in gas phase consists of the fully three-dimensional, transient equations of mass, momentum, energy and species conservation. For clarity, only the most relevant mathematical models for the present water mist simulation are described here. The governing equations for both the gas and the droplet phases are discretized and iteratively solved, and a detailed description is given in FDS user guide [13].

Lagrangian Particle Model

The droplet model such as a Lagrangian approach consists of the droplet evaporation and the rates of change in vapor mass/in the droplet temperature and in the gas temperature. The drop size distribution is characterized by Cumulative Volume Fraction, which agrees well with the Rosin-Rammler-lognormal curve [13].

In the gas phase, the momentum lost from a particle is added to the fluid and vice versa through the drag force.

$$\mathbf{f}_b = m_d\mathbf{g} - \frac{1}{2}\rho C_d A_d \left(\mathbf{u}_d - \mathbf{u}\right)\left|\mathbf{u}_d - \mathbf{u}\right| \qquad (1)$$

where A_d refers the particle cross-sectional area, ud the particle velocity, md the particle mass, u the gas velocity, ρ the gas density and g the gravitational acceleration.

The acceleration of a single spherical droplet is given by

$$\frac{d\mathbf{u}_d}{dt} = \mathbf{g} - \frac{1}{2}\frac{\rho C_d A_d}{m_d}\left(\mathbf{u}_d - \mathbf{u}\right)\left|\mathbf{u}_d - \mathbf{u}\right| \qquad (2)$$

The parameter C_d in Eqs.(1, 2) represents the drag coefficient between the liquid droplet and the gas, and is a function of the droplet Reynolds number, Re_d.

$$C_d = \begin{cases} 24\,Re_d^{-1} & \text{for } Re_d < 1 \\ 24\left(0.85 + 0.15\,Re_d^{0.687}\right)Re_d^{-1} & \text{for } 1 < Re_d < 1000 \\ 0.44 & \text{for } Re_d > 1000 \end{cases} \qquad (3)$$

$$Re_d = \frac{2r_d|\mathbf{u}_d - \mathbf{u}|}{\mu} \qquad (4)$$

where r_d is the particle radius and μ the dynamic gas phase viscosity

Drag Reduction

It is worth noting that in a Lagrangian approach, the particles occupy no volume in the Eulerian space, and the separation lengths would be of sub-grid scale. As a consequence, in a dense water spray, aerodynamic interactions between the individual particles cannot be captured explicitly by the current Eulerian-Lagrangian model. The separation distance is obtained from the local particle volume fraction, α_d [13]:

$$\frac{L_d}{2r_d} = \left(\frac{\pi}{6\alpha_d}\right)^{1/3} \qquad (5)$$

Since local quantities are averaged over a single computational cell, the aerodynamic interactions become significant when the ratio of the inter-particle spacing (Ld) to the particle diameter ($D=2r_d$), L_d/D, is less than 10. The reduction of the drag force on the second particle in a dense water spray is modeled as [13] :

$$C_d = C_{d,0}\frac{F_d}{F_{d,0}} \qquad (6)$$

where $C_{d,0}$ is the single particle drag coefficient and $F_d/ F_{d,0}$ is the hydrodynamic force ratio of the trailing particle to an isolated particle:

$$\frac{F_d}{F_{d,0}} = W\left[1 + \frac{Re_d}{16}.\left(\frac{L_d}{2r_d} - \frac{1}{2}\right)^{-2}.\exp\left(-\frac{Re_d}{16}.\mu.\left(\frac{L_d}{2r_d} - \frac{1}{2}\right)^{-1}\right)\right] \qquad (7)$$

where W is the non-dimensional, non-disturbed wake velocity at the center of the trailing particle, defined as:

$$W = 1 - \frac{C_{d,0}}{2}.\left[1 - \exp\left(-\frac{Re_d}{16}.\left(\frac{L_d}{2r_d} - \frac{1}{2}\right)^{-1}\right)\right] \qquad (8)$$

In the simulation, the drag reduction factor in Eq.(7) is only activated when the local droplet volume fraction, α_d, exceeds 10^{-5}.

Combustion Model

Although the combustion chemistry of a fire-water interaction is expected to be complex, a more robust four-step chemistry scheme is assumed for the oxidation of heptane and soot in flame [15].

$$C_7H_{16} + 10O_2 \rightarrow 6\,CO_2 + 7\,H_2O + CO + H_2 \qquad (9)$$

$$2\,CO + O_2 \overset{H_2O}{\longleftrightarrow} 2\,CO_2 \qquad (10)$$

$$2\,H_2 + O_2 \leftrightarrow 2\,H_2O \qquad (11)$$

Effects of finite-rate kinetic reactions on ignition processes of gas phase combustion attached to the fuel type greatly complicate the numerical modelling. Therefore, a mixing-controlled infinitely fast chemistry approach is employed for the primitive fuel combustion (Eq.9).

$$\dot{\omega}_i''' = \rho\left[\frac{\zeta(t)}{\tau_{mix}}(Y_i - Y_i^0) + (1 - \zeta(t))\frac{dY_i}{dt}\right] \quad \text{and} \quad \zeta(t) = \zeta_0 \exp(-t/\tau_{mix}) \qquad (12)$$

where τ_{mix} denotes key mixing timescale, ζ(t) the unmixed fraction at time step t, and the initial value of unmixed fraction, ζ_0, is set to 1. The rate of change in the mass fraction of species i in the mixed reactor zone, $\frac{dY_i}{dt}$ can be determined by summing the mass rate of the reaction per unit volume for species i across all chemical reactions. Eq.12 is combined with a finite-rate Arrhenius reverse chemistry to create a mixed reaction. The exothermic reaction of carbon monoxide oxidation and the reversible endothermic reaction of CO2 (Eq.10) are expressed as follows:

$$\dot{\omega}_{CO}''' = -1.5 \times 10^9 T^0 e^{-41840/RT}[CO][O_2]^{0.25}[H_2O]^{0.5} \qquad (13)$$

$$\dot{\omega}_{CO2}''' = -6.16 \times 10^{13} T^{-0.97} e^{-328026/RT}[CO_2][O_2]^{-0.25}[H_2O]^{0.5} \qquad (14)$$

The presence of the water vapor in Eq.10 for CO oxidation (Eq.13) and CO2 dissociation (Eq.14) is required, but its concentration does not explicitly participate in the reaction. The hydrogen combustion with oxygen is formulated as :

$$\dot{\omega}_{H2}''' = -8.5 \times 10^{15} T^{-1} e^{-167360/RT} [H_2]^{0.25} [O_2]^{1.5} \quad (15)$$

The rate of the corresponding reverse water vapor (H_2O) dissociation is obtained from equilibrium [13]. It is worth noting that in FDS6 [13], interaction between turbulence and finite-rate chemistry is not incorporated. If an infinitely fast chemistry approach (Eq.12) is prescribed in the chemistry equations 10 and 11, the CO and H_2 productions are almost suppressed.

Radiation and Soot Models

Radiation Transfer Equation (RTE) is solved with a ray-based method [13] in angular discretization and a finite volume method in spatial discretization. The absorption coefficient in the RTE includes gas-phase radiation of the most important combustion product controlling the thermal radiation, such as H2O, CO, CO2, soot and water mist. The laminar smoke-point (LSP) [16] is widely adopted as a quantitative measure of the sooting tendency of fuels, and soot formation rate can be well correlated by LSP. The soot nucleation rate is determined as follows :

$$\dot{\omega}_{s,N}''' = A_f \rho^2 T^{2.25} \frac{f - f_{st}}{1 - f_{st}} \exp(-2000/T) \quad (16)$$

Here, ρ denotes volume density (kg.m^{-3}), T (K) gas temperature, and f mixture fraction. The pre-exponential factor A_f, deals with the fuels sooty propensity with reverse proportionality relationship with the smoke height L.

$$\frac{A_{f,Fuel}}{A_{f,C_2H_4}} = \frac{L_{C_2H_4}}{L_{Fuel}} \quad (17)$$

The A_f for ethylene has been initially calibrated to be 4.1x10^{-5}, and for heptane is Af =2.9x10^{-5} for a smoke height of L=0.147 m. The surface growth rate determined from gas temperature, T, soot number density, N, and mole fraction of the hydrocarbon, X_F.

$$\dot{\omega}_{s,G}''' = C_\gamma \rho T^{1/2} X_F \exp(-T_\gamma/T)\ N^{1/3} (\rho Y_s)^{2/3} \quad (18)$$

The empirical parameters, C_γ and T_γ , are experimentally calibrated in a non-premixed flame.

Once the soot leaves the active flaming region, its oxidation is likely to be surface area controlled. Several species have been linked to soot oxidation in hydrocarbon diffusion flames, most notably O2, O and OH radicals. The soot oxidation reactions collectively sum to the temperature dependence as a function of soot and oxygen concentrations (mol/cm^3) [13].

$$\dot{\omega}_{s,O}''' = -4.7 \times 10^{10} [Ys][Yo] \exp(-211000/RT) \quad (19)$$

Here, R denotes the gas universal constant.

Heat and Mass Balances at Interface

The heat balance is established on the front surface to calculate the surface temperature of liquid through the convective and radiative heat fluxes.

$$-k_s \frac{\partial T_s}{\partial x}(0,t) = \dot{q}_{conv}'' + \dot{q}_{rad}'' - \dot{m}_s'' L_v \quad (20)$$

where the point x=0 represents the surface of liquid. A one-dimensional heat conduction equation for the thermally-thick condensed phase temperature $T_s(x, t)$ is applied in the direction x pointing into the liquid phase. The radiation heat flux is calculated from the radiation intensity by solving RTE [13]. The wall model for velocity is used, which is based on the law with a semi-log fit connecting the limits of the viscous and log regions. By analogy to the near-wall model for velocity, the convective heat flux at the liquid surface is obtained from the non-dimensional temperature scale and the resistance to the heat and momentum transport close to the wall [13].

The evaporation rate of liquid fuel is calculated from the Stefan equation [13].

$$\dot{m}_F'' = \frac{\rho D}{L} N_u Ln\left[\frac{1 - Y_{F,\infty}}{1 - Y_{F,i}}\right] \quad (21)$$

where D denotes the mass diffusivity, L the length scale and Nu Nusselt number. Mass fraction of fuel vapor at the interface is found from a Clausius-Clapeyron relation with a dependence on its surface temperature, T_s, and boiling temperature, T_b.

$$Y_{F,i} = \frac{W_F}{W_m} \exp\left[-\frac{L_v W_F}{R}\left(\frac{1}{T_s} - \frac{1}{T_b}\right)\right] \quad (22)$$

Here ,W_F /W_m denotes molar weight of liquid fuel/mixture and L_v pyrolysis heat. Recirculation in the liquid phase is not taken into account.

Computational Domain and Boundary Conditions

According to the experimental configuration (Fig.1), the three dimensional computational domain of 2x2x2.5 m^3 in the x, y and z directions respectively, is chosen. Such a calculation domain is large enough to exclude the negative effect of boundary entrainment on flow field. The liquid surface is 23 cm in diameter and is embedded in the z=0 plane, centered in the x, and y directions. Zero gradient conditions are used for the far-field free boundary values of the variables. A mesh size optimization, which is based on the fire characteristic length spreading over about sixteen computational cells [13], is meaningful only for the calculation of the fluid motion outside the flame zone.

An extremely small grid size lower than 1 mm is required to fully resolve the flame thickness and turbulent flow instabilities, making practical fire simulations difficult. The regular Eulerian grid contains 100x100x150 grid cells, and the finally chosen grid size in an order of 1 cm around the fire source usually gives grid-independent prediction for the most three-dimensional turbulent fire simulations [13]. By using 16 processors through parallel processing of a Linux cluster, the CPU time for a simulation with a physical time of about 120 s is approximately 100 h. The local speed and Sauter Mean Diameter were measured at a distance of 70 cm from the nozzle exit by using a laser anemometry system as PDPA (Phase Doppler Particle Analyser). Droplet diameter of about 50μm and an injection velocity of 10 m/s at the nozzle exit are numerically calibrated and used at the nozzle exit as an input in the simulation by using FDS6 [13].

Results and Discussions

As shown in Fig.2, before activation of water mist, an abrupt increase of the HRR in an initial transient period is followed by a subsequent progressive increase. Starting from 40 s, the fire becomes fuel-controlled which is limited by heat feedback from the flame to liquid fuel surface. A fully developed, quasi steady state is reached with a plateau in the HRR of about 36 kW close to the experimentally determined one. Since water droplets influences the weight of the fuel pan once the water spray system is activated, the HRR cannot be derived from the measured mass loss rate of fuel. Water mist with a rather high momentum is applied at t0=60 s. It appears that such mist provides an unsuppressed flame condition, and a higher HRR of 66 kW is achieved after activation of water mist. This is attributed to the buoyancy-induced rising plume which is sufficient to deflect the water mist spray. An interplay of the gas-phase combustion within the water mist cloud induces a stronger oscillation of the HRR.

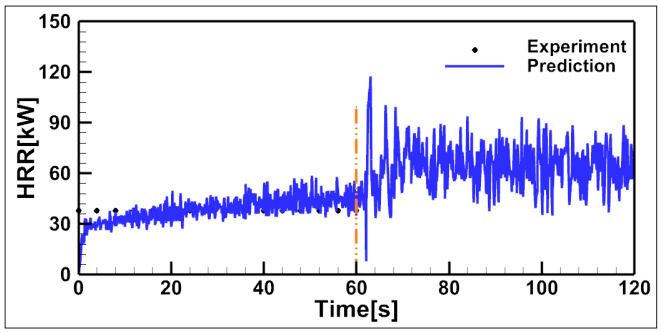

Figure 2: Impact of Water Mist on Evolution of The Predicted Heat Release Rate

Water vapor changes significantly the physical effects (expansion, dilution, heat capacity), and is also chemically active. Qualitative instantaneous images from a CCD camera are presented in Fig.3 to depict a time-varying visible flame oscillation which is characterized by a flame necking phenomenon and the intermittent zone. The injection of finely divided water mist (50µm) at t0=60 s into a flame has a combustion-supporting effect. This results in rapid evaporation and expansion leading to a total destruction of the flame with random lateral ejection of reacting hot gaseous pockets at t=t0+5 s. The droplets disturb the turbulent flame structure with the occasional wisp of flame at the top of the reactive zone that escape the water mist cloud nearby the fire source. The reason for flame expansion is attributed to penetration of droplets, in all regions of the flame, and of their rapid evaporation and expansion which causes gas displacement in the vicinity. Application of water mist precedes only partial fire extinguishment at t=t0+10 s with a reduction in the flame size.

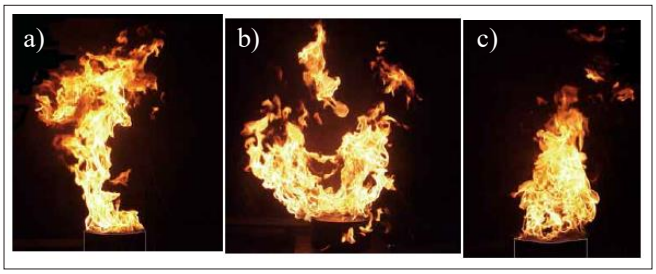

Figure 3: Instantaneous Flame Images During Interaction Between Fire and Water Mist with Application Time at t0=60 s (a), t=t0+5 s (b) and t=t0+10 s (c)

Both experiment and prediction show in Fig.4(a, b) that without water mist, the overall time-averaged temperature distributions are well characteristic of those encountered in diffusion flames with a maximum temperature at the edge indicating the presence of high reactivity.

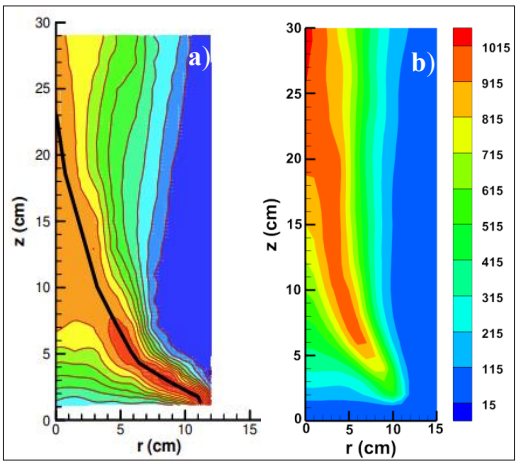

Figure 4: Measured (A) and Predicted (B) Time-Averaged Temperature Distribution in No Water Mist Case

The predicted and measured temperature profiles along the flame axis at the four radial positions (r=0, 3, 6, 9 cm), are presented in Fig.5 before activation of water mist. There is a good fit between the predicted and measured gas temperature without water mist.

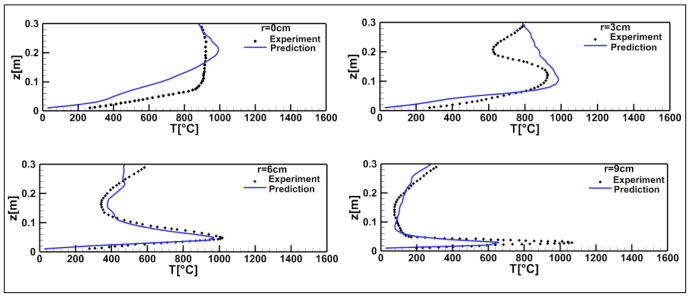

Figure 5: Comparison of Predicted and Measured Axial Temperature Along the Four Thermocouple Trees in No Mist Case

As shown in Fig.6, after application of water mist, mixing and reaction processes are random in time and space and the distinction between rich and lean regions becomes ill-defined due to the volumetric expansion effect of water mist. Therefore, time-averaged temperature field from the instantaneous flame structure (Fig.3), as those obtained in Fig.6, cannot be expected to give deeper insight into the detailed mechanisms. Under conditions of water vapour addition, the maximum temperature is moved toward the pyrolysis surface. The computed temperature field is with a visual similarity compared to the measured flame structure. The observed phenomenon is partly a temperature effect, via activation energies associated with the water–gas shift reaction downstream of the flame. The addition in droplet evaporation enhances buoyancy and shifts the region of high reactivity, inferred by the temperature distribution from the burning surface. The effect may be essentially related to the absorption of a part of the combustion energy because water vapour behaves as an inert diluent and heat sink. It is most probable that there are two competing effects such as a cooling effect due to the addition of significant amounts of water vapour which play the role of heat sink and an exothermic effect associated with the shift of the water gas reaction toward CO2.

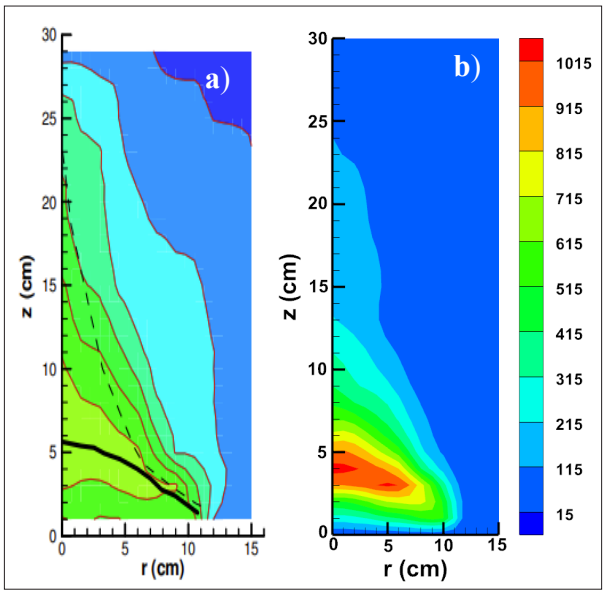

Figure 6: Measured (A) and Predicted (B) Time-Averaged Temperature Distribution During Interaction Between Fire and Water Mist

Profiles of the predicted and measured axial temperature along the four thermocouple trees (r=0, 3, 6, 9 cm) after application of water mist are presented in Fig.7. It is worth noting that the general characteristics of the predicted evolutions are in qualitative agreement with the measurements of gas temperature. The water droplets evaporate well before approaching the flame sheet, and a consecutive efficient cooling of the thermal plume can't reduce the flame temperature below a critical temperature of 400°C necessary to sustain combustion. The temperature magnitude depends on both the flame radiation due to the increase of water vapour concentration within the flame, and the decrease due to less soot formation. Although the validation of the temperature profiles is just qualitative, it does provide a good indication of the impact of the mist on the macroscopic variables of the process, such as the thermal field.

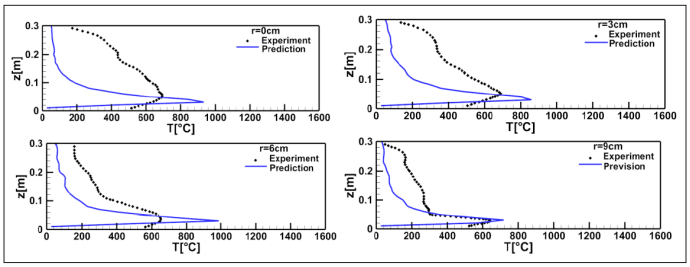

Figure 7: Comparison of Predicted and Measured Axial Temperature Along the Four Thermocouple Trees After Application of Water Mist

As shown in Fig.8, the pyrolysis rate asymptotically reaches a limit to supply a permanently burning flame once the liquid temperature is established at a steady state over liquid surface. The expansion effect of the water vapour shifts the region of high reactivity towards the burning surface, and an enhancement of the burning rate is related to the significance of convective heat flux. The sharp increase in the flow of volatiles gives rise to a strong mixing between heptane vapour and entrained air, resulting in a convective type of mixing rather than from a purely diffusive one, which gives to the reaction zone a premixed rather than a diffusive character at its base, as shown in Fig.3. The pyrolysis rate remains uniform over the burning surface except with a sharp decreases near the edge of the pool fire due to a decreasing trend of the liquid temperature.

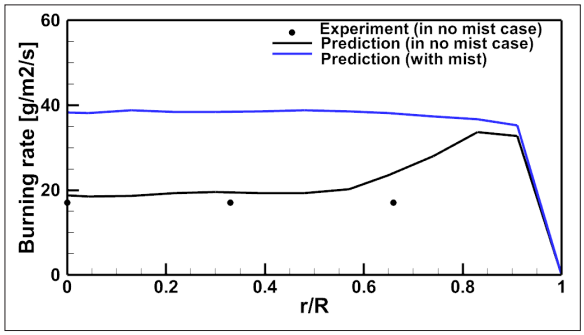

Figure 8: Evolution of The Pyrolysis Rate Along the Burning Surface Before and After Application of Water Mist

It would be worthwhile to analyse the resulting radiant emission from the flame which in turn determines the burning rate. The radiative flux is a temperature-sensitive volumetric mechanism associated with both the gas temperature and concentration of emitting species as CO_2, H_2O and soot. As shown in Fig.9, the radiation heat flux gives a peak in heat flux of about 15 kW/m^2 without water mist. A high radiative heat flux covers the entire pyrolysis area because a larger flame zone yields substantial soot and luminous radiation. Application of water mist conducts to a decrease of radiative heat flux to 10 kW/m^2. The deviation of the numerical results in relation to the measured radiative heat flux is within 50% mainly due to over-prediction of the gas temperature around the fire source (Fig.7).

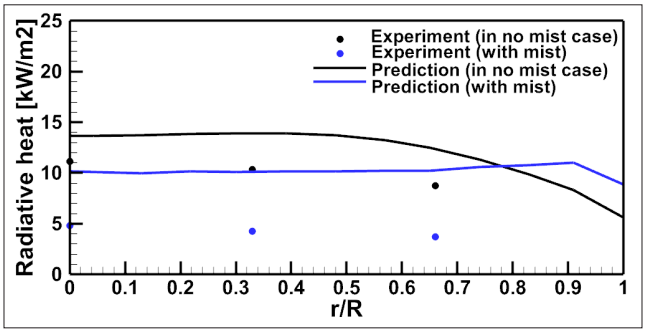

Figure 9: Evolution of The Radiation Heat Flux Over the Pyrolysis Surface Before and After Application of Water Mist

The convective heat exchange from the flame to the liquid surface is shown in Fig.10. Before activation of water mist, the convective heat flux exhibits a peak of about 6 kW/m2 at the edge of flame base due to strong interaction between buoyancy-induced flow and fuel injection. A sharp decrease to about 1 kW/m2 far away from that region is a result of a reduction in temperature gradient in center of the pyrolysis zone where the flame is significantly lifted above the fuel surface. There is a greater convective heat flux by applying water mist in center of the pyrolysis zone with an increase by a factor of five times compared to that in no mist case.

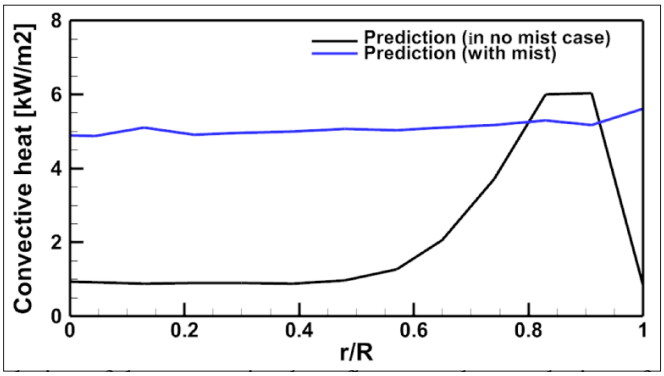

Figure 10: Evolution of The Convection Heat Flux over The Pyrolysis Surface Before and After Application of Water Mist

A typical example of the distribution of carbon monoxide concentration (mol/mol) on the symmetrical plane (x, z) is presented in Fig.11(a, b). In no mist case (Fig.11a), the buoyancy-induced flow carries abundant CO along the forward flow with a slow decay of the CO emission. After application of mist, the flame allows to entrain more water vapour which is capable of providing a quick decay of the CO emission in a thermal plume region. It seems that the peak in CO molar fraction is weakly dependent on water mist with a maximum of roughly 1% which is indicative of an equivalent fuel-air ratio in the reaction region. It is somewhat expected that the conditions of water vapour addition are favour to a maximum chemical effect, and water mist addition should decrease the CO concentration and enhance CO2. However, the prediction (Fig.11b) indicates that the dilution effect appears significantly larger than the chemical one. In reality, since the competing reactions involving H2, CO and soot are coupled with water mist addition, the interpretation from the numerical results can only be of qualitative and speculative nature. No measurements and predictions are made of the radicals and other species present in the flame with activation of water mist. In addition, there are rather complex combinations of mixing and reaction processes with water mist addition, neither of which are stationary in space and time. Usually, CO and soot formations are closely related with existing of obvious kinetic links between them [14].

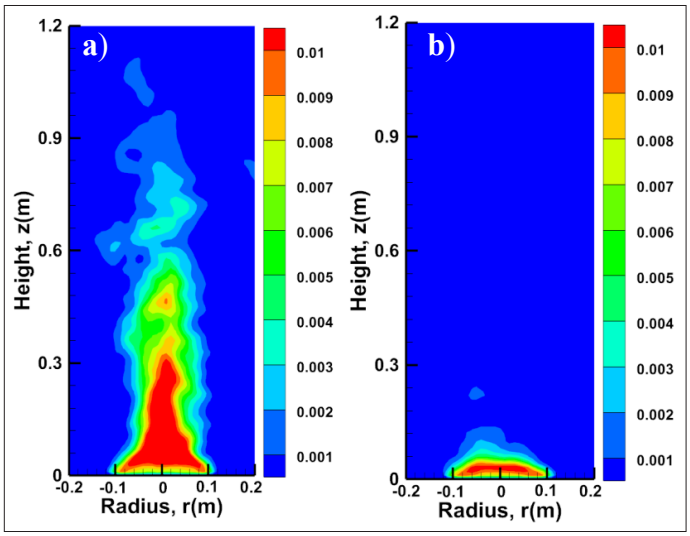

Figure 11: Distribution of The Predicted Co Concentration Before (A) and After (B) Application of Water Mist

Iso-contours of hydrogen concentration (mol/mol) on the symmetrical plane (x, z) are depicted in Fig.12(a, b). In no water mist case, a buoyancy-induced fire (Fig.12a) correlates to a large extent of a H_2 concentration above 0.5% in the high temperature region. In this context of water vapour addition in a hot environment, it is expected that H_2 increases and H_2O decreases. Application of water mist significantly reduces the extent of H_2 concentration above 0.5% due to a decrease in reaction temperature (Fig.6). It is found that the maximum H_2 undergoes an increase only in fuel rich region when the temperature is sufficiently high, and later, enters quickly the decay phase. The extent of H_2 production in no mist case increases by a factor of ten times compared to that by activating water mist. Globally, hydrogen occurs only in the fuel-rich, an oxygen-starved area at locations where the temperature is high enough to trigger its activation. It is worth noting that H2 is highly flammable with an ignition energy that is smaller than that of unburnt hydrocarbons [14].

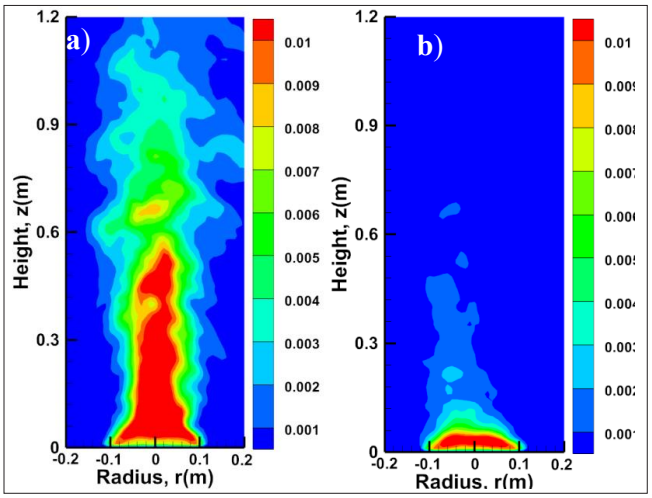

Figure 12: Iso-contours of the predicted Hydrogen Concentration Before (A) and After (B) Application of Water Mist

Iso-contours of unburnt hydrocarbon concentration (mol/mol) as heptane on the symmetrical plane (x, z) are depicted in Fig.13(a, b). The most severe production of unburnt fuels with a peak of about 10% nearby the pyrolysis zone is mainly attributed to the under-ventilated condition due to lack of oxygen. With application of water mist, the unburnt hydrocarbons can be easily suppressed downstream once away from the fuel rich region of fire source. However, a water vapour addition heavily restrict fresh air supply into the pool fire base, leading to again a strong molar fraction of the unburnt hydrocarbons regardless of the dilution effect. Usually, the soot precursory rate strongly correlates to concentration of the unburnt hydrocarbons regardless of water vapour addition.

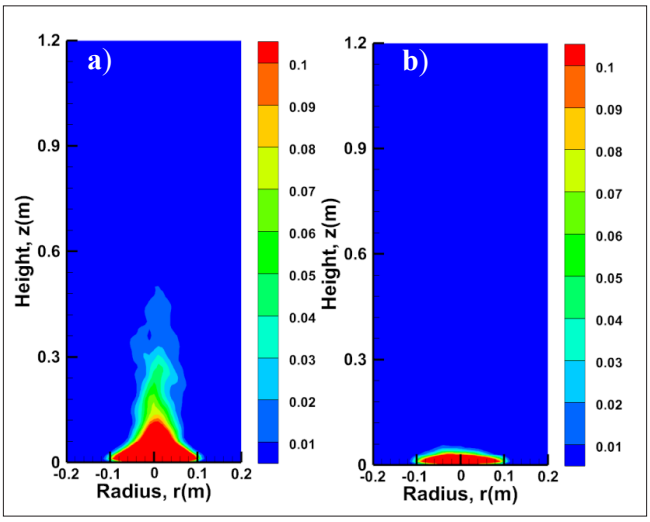

Figure 13: Iso-contours of the Predicted Unburnt Hydrocarbon Concentration Before (A) and After (B) Application of Water Mist

Iso-contours of the predicted soot volume fraction (ppm) before and after activation of water mist on the axis of symmetry are depicted in Fig.14(a, b). In no mist case, the concentration of soot is low near the liquid surface due to the quasi-absence of oxidant species penetration for any reaction of fuel vapour and pyrolysis products. The majority of soot emission takes place downstream in the fuel-rich core where heat is released as the fuel reacts with the entrained air. Natural convection is favorable for dilution in the thermal plume with a decreasing trend in soot emission peak. After activation of water mist, reduction in soot emission is significant, and the majority of soot formation takes place at the bottom of the fire. The highly reactive radicals induced by water mist react quickly with hydrocarbon species causing an effective reduction in the rate of soot initiation and growth and resulting in an inhibiting effect. Soot emission in the thermal plume is suppressed as soon as the mist-plume interfaces approaches the flame sheet.

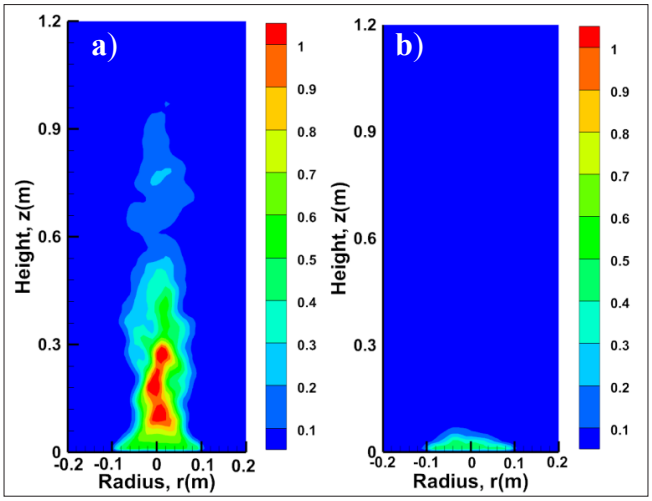

Figure 14: Iso-contours of The Predicted Soot Concentration Before (A) and After (B) Application of Water Mist

The predicted and measured soot volume fraction in no mist case at the height of h/D=1.5 and 3.4 above the base of a heptane fire are compared in Fig.15. Soot volume fraction distribution is globally in good agreement with experimental data. The computed profiles of RMS soot volume fractions, $\sqrt{(f_v'^2)}$, are compared with experimental data in Fig.16. The predicted RMS soot volume fraction is significantly lower than the experimentally estimated value at the location of h/D=3.4, corresponding to a higher intermittent region. A simple calibration of the soot empirical parameter for matching the measured results is insufficient. Globally, the uncertainty in the prediction of soot formation in Fig.14 is estimated within 30-40%.

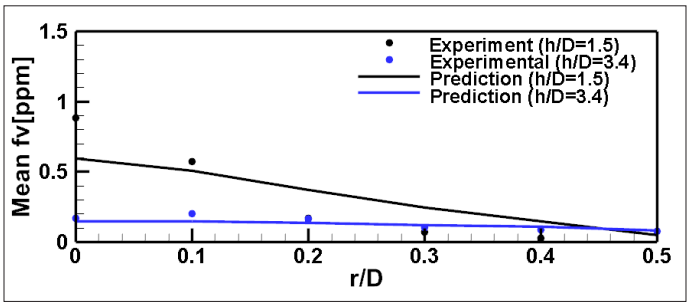

Figure 15: Comparison Between Measured and Predicted Soot Volume Fraction in No Mist Case

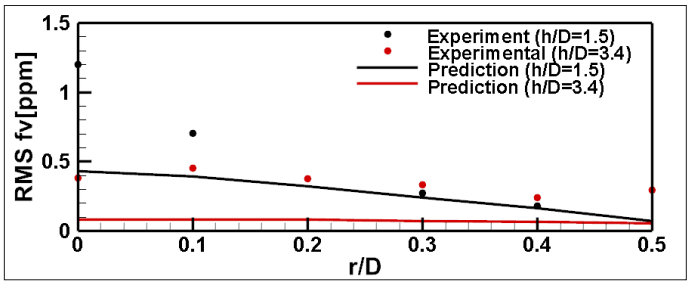

Figure 16: Measured and Predicted Rms Soot Volume Fraction in No Mist Case

Conclusions

An experimental and numerical study on the suppression of a turbulent diffusion flame by applying water mist has been conducted. This numerical study has provided an in-depth analysis on the impact of water mist on the thermal expansion and chemical species distribution. In comparison with the experimental data, the uncertainty in the prediction of fire suppression by water mist is estimated within 20-30% by taking into account a multitude of potential errors in combustion, soot and drag force models. An improved prediction of the flame structure emphasizes the need for developing advanced numerical models for the drag reduction effect on water mist sprays [16,17].

The present study corroborates that the presence of water vapour has a significant dilution effect on a flame structure in addition to heat sink and enhanced mixing resulting in volumetric expansion. The water mist leads to mainly influence physical phenomena, especially in reducing the resultant flame temperature. The numerical results do not allow to point to evidence that water vapour interacts chemically in the flame, such as a decrease of soot, CO and an increase of CO_2 with increasing water vapour addition. The explanation of the observed mist effects from the present case is of a purely speculative nature as no measurements and prediction are made of the radicals or other species present in the flame. In order to clarify this chemical effect of water vapour on diffusion flame, OH* or other radical measurements or prediction should be of particular importance. The future study aims to calls upon new developments for droplet aerodynamic modelling in water mist sprays because of the perturbing influence of the injected water vapour at the flame base.

References

1. Liu Y, Wang X, Liu T, Ma J, Li G, et al. (2020) Preliminary study on extinguishing shielded fire with water mist. Process Saf. Environ. Prot 141: 344-354.
2. Liu Z, Kim AK (2000) Review of water mist fire suppression systems – fundamental studies. J Fire Prot Eng 10: 32-50.
3. Jenft A, Boulet P, Collin A, Trevisan N, Mauger PN, Pianet G (2017) Modeling of fire suppression by fuel cooling. Fire Saf J 91: 680-687.
4. Grant G, Brenton J, Drysdale D (2000) Fire suppression by water sprays. Prog. Energy Combust Sci 26: 79-130.
5. White JP, Verma S, Keller E, Hao A, Trouvé A, Marshall AW (2017) Water mist suppression of a turbulent line fire. Fire Saf J 91: 705-713.
6. Liu Y, Fu Z, Zheng G, Chen P (2022) Study on the effect of mist flux on water mist fire extinguishing. Fire Saf J 130: 103601.
7. Ananth R, Ndubizu C, Williams F (2004) A numerical model for water mist suppression of a solid plate in boundary layer flow. In: Halon Options Technical Working Conference. NMERI 1-10.
8. Mehaddi R, Collin A, Boulet P, Acem Z (2020) Use of a water mist for smoke confinement and radiation shielding in case of fire during tunnel construction. Int J Therm Sci 148: 106156.
9. Dasgotra A, Rangarajan G, Tauseef SM (2021) CFD-based study and analysis on the effectiveness of water mist in interacting pool fire suppression. Process Saf Environ Prot 152: 614-629.
10. Yao Y, Li YZ, Ingason H, Cheng X, Zhang H (2020) Theoretical and numerical study on influence of wind on mass loss rates of heptane pool fires at different scales. Fire Saf J 120: 103048.
11. Jenft A, Collin A, Boulet P, Pianet G, Breton A, Muller A (2014) Experimental and numerical study of pool fire suppression using water mist. Fire Saf J 67: 1-12.
12. Ingason H, Li YZ (2019) Large scale tunnel fire tests with different types of large droplet fixed firefighting systems. Fire Saf J 107: 29-43.
13. McGrattan K, Hostikka S, Floyd J, McDermott R, Vanella M, Mueller E (2024) Fire Dynamics Simulator User's Guide. 6th ed. NIST Special Publication: 1019.
14. Kanury AM (1984) Introduction to Combustion Phenomena. New York: Gordon.
15. Richard J, Garo JP, Souil JM, Vantelon JP (2003) On the determination of soot and droplet concentration and velocity fields during the addition of a water mist on a liquid pool fire at laboratory scale. In: Seventh International Symposium on Fire Safety Science. Worcester Polytechnic Institute, U.S.A. 7: 507-518.
16. Yao W, Zhang JP, Nadjai A, Beji T, Delichatsios MA (2011) A global soot model developed for fires: Validation in laminar flames and application in turbulent pool fires. Fire Saf J 46: 371-387.
17. Lee KB, Thring MW, Beer JM (1962) On the rate of combustion of soot in a laminar soot flame. Combust. Flame 6: 137-145.